Size-dependent synergetic seeding effects in the inspection of airborne dry nanoaerosols by LIBS

P. Purohit[a], F.J. Fortes[a]*, I. Malegiannaki[b], L. Jaime-Fernández[a], J.J. Laserna[a]

[a] UMALASERLAB, Departamento de Química Analítica, Universidad de Málaga, C/Jiménez Fraud 4, Malaga 29010, Spain.

[b] Department of Chemistry, University of Crete, GR 710 03, Heraklion, Crete, Greece.

ABSTRACT

In the present paper, confined dry Cu nanoaerosols of controlled particle size are inspected under a time-resolved LIBS scheme to explore the effect of laser-particulate matter interaction upon the detection capability of airborne nanoparticulate material. Optically catapulted streams probed showed linear intensity vs mass correlation and similar signal stability which is linked to the seeding effect caused by smaller particles yielding hotter, albeit shorter plasmas. Seeding effect is demonstrated by hyperspectral time-resolved aerosol inspection, which exposes both, the interaction between multiple plasma nuclei and the discrete nature of the laser-particle interaction. Observed population/exhaustion cycles at the focal volume of the inspection laser explained the uncertainty values characteristic of LIBS inspection of aerosols. A thorough inspection of the emission in time evidenced a significantly different evolution of the intensity profile for commonly monitored Cu lines owed not only to the nature of the monitored transit and pulse energy, but also to particle size. These results suggest that the experimental settings for quantitative ultrafine aerosol inspection need to be tuned according to the target particle size and the particle density of the aerosol as seeding effects facilitates signal saturation, therefore this effect simultaneously contributes to and detracts from the analytical performance of LIBS on nanometric aerosols.

* Corresponding Author: F.J. Fortes, Phone +34951953015, E-mail: javierfortes@uma.es

Keywords: Nanoaerosol inspection; Optical Catapulting; LIBS; Airborne particles; Hyperespectral imaging; Laser-Nanoparticle Interaction

1. Introduction

The direct correlation existing between air quality and quality of life has turned the monitoring of airborne biological and chemical species both in industrial environments and urban nuclei a major concern [1-3]. Historically, a variety of analytical techniques have been employed to determine the chemical composition of atmospheric particulate matter. Nowadays, sensors based on methods that allow real-time field analysis are the most demanded and encouraged for this application.

Among spectroscopic techniques, laser-induced breakdown spectroscopy (LIBS) has been especially successful for characterizing airborne particulate material [4-6]. LIBS has reached an outstanding degree of instrumental and methodological maturity that has allowed it to adapt to increasingly complex analytical problems. The inspection of planetary surfaces, submerged samples, isotopic analysis or single nanoparticles (NPs) illustrate extreme scenarios already accessible to LIBS. The scarce sample quantity required to perform an analysis alongside the possibility of detecting multiple elements in a single event make LIBS a strong contender for the direct inspection of aerosolized matter in-lab as well as off-lab [7-9]. For particles with diameters (d) higher than 100 nm, that is, belonging to the fine and coarse fraction of particulate matter, limits of detection (LODs) as low as 3 femtograms in absolute mass have been reported for 175 nm Ca- and Mg-based particles [10] along concentration LODs of 0.3 μg/L [11]. A common drawback tied to aerosol inspection in a low percentage of real hits, i.e., low number of spectra exhibiting emissions tied to the analytes, consequently leading to high relative standard deviations (RSDs), often ca.30-50%. This is particularly true when wet aerosols are probed as, provided the absence of secondary drying sources, the impinging laser light

is forced not only to invest part of its energy in drying the particle, but also to traverse an atmosphere-water interphase. The change of the refraction index in the interphases causes a slight focus shit due to lensing effect implying that the energy reaching the particle is further decreased. Conditional spectral processing schemes have been demonstrated as a reliable solution for lowering the uncertainties tied to aerosol analysis [12], thus dramatically improving the performance of LIBS on these samples to the point of allowing standoff instruments to be deployed in an industrial plant to assess the particles to which workers were exposed [13].

In spite of the positive results, the ultrafine fraction (UF), of d < 100 nm, is still elusive for LIBS and significantly less papers have been devoted to targeting it despite their clear impact upon health and the environment they are released to [14]. The combination of optical catapulting (OC) and LIBS is one of the methods proposed for the characterization of NP aerosols and was developed in a series of works by Fortes et al. [15-17]. Working directly with dry aerosols was one main advantage of OC-LIBS as RSDs values were significantly reduced in this approach with sampling throughputs of ca.90% real hits. This hyphenated technique played a major role in the posterior development of the single NP strategies mentioned above. Key details concerning laser-particle interaction have derived from the research performed on single NP-LIBS which, in turn, can nurture aerosol inspection as new insight may be used to target UF nanoparticles [18-21]. Of remarkable importance are data indicating the energy regime under which NPs are expected to be detected, the possible interferences coming from surrounding air ionization as well plasma lifetime and physical traits, which are largely affected by seeding effects, since the combination of these points end up determining which lines may be used for successfully running UF experiments [22]. Higher emission intensity lines are often employed in LIBS aerosol inspection as the discrete nature of the

laser-particle interaction often lead to low signal-to-noise ratios (SNR) sought to be improved on the basis of optimized monitored line choosing. Yet, these emissions are prone to non-linearity with relative ease due to particle size, especially in the case of particle clustering, high pulse energy, as off-lab experiments tend to use energies closer to the maximum laser output, or background impact upon the recorded signal if the acquisition window is not fully optimized, as may happen with the time-integrated spectrometers commonly found in the detection system of instruments built for in-situ analysis. Therefore, quantitative studies transcending the controlled boundaries imposed in ad-hoc laboratory UF inspection may be greatly hindered if the multiple processes comprised by the mechanisms leading to the dissociation of the particles and the subsequent excitation of the free atoms are not carefully addressed.

In the present work, time resolved inspection of confined dry nanoaerosols featuring Cu nanoparticles of controlled average diameter produced by optical catapulting is performed in order to elucidate the impact of particle size upon the LIBS inspection of the aerosols. The evolution of resonant lines at 324.75 and 327.4 nm, largely used for the detection of Cu in primary and secondary aerosol production sources, is compared to that of the 510.55, 515.32 and 521.74 nm lines. This triplet possesses an intensity ratio which has been demonstrated to hint the number of particles probed in the case of low particle densities. Plasma lifetimes are measured as a function of particle size and explained on the basis of plasma electronic temperature (T_e). Optimal time frame for intensity vs diameter correlation is given. LIBS shot-to-shot signal stability is studied for the 324.75 and the 521.74 nm emission along with simultaneous time-resolved hyperspectral imaging seeking to both explain the origin and diminish the RSD value of UF inspection. The behavior of the two lines for increasing pulse energy values is monitored with intensity ratios calculated to establish a correlation between recorded signal and available

excitation energy. Lastly, known amounts of the three particle diameters inspected herein are probe to set the most appropriate line to monitor as a function of particle size and absolute mass present within the sample inspection chamber.

2. Experimental

2.1. Instrumentation

The custom-made experimental setup employed herein is depicted in **Fig. 1 A and B**. The instrument integrated two Nd:YAG lasers working at their fundamental wavelength (λ = 1064 nm, TEM 00) with pulse width of 6 ns. One of the lasers was devoted to the formation of dry aerosols via OC (UL120211, Big Sky, USA) while the other was used to perform the LIBS (SL284, Spectron, UK) characterization of the particle stream. As shown in Fig. 1A, the OC laser was guided into a 20x long working distance microscope objective (N.A. = 0.40, TU Plan ELWD, Nikon, Japan) placed in the z axis. The pulse was focused 2.5 mm below the optically transparent bottom of the sample chamber (detailed in subsection 2.2) and a pulse energy of 7 mJ was used to produce a shockwave that caused the ejection of the NPs upon reaching the chamber. By using this approach, homogeneous and reproducible nanoaerosols of low particle density were created coaxially in the direction of light propagation. Energy density (F = J/cm^2) for OC was kept below plasma formation threshold for glass (F = 9.5 J/cm^2) in order to preserve both, the microscope objective and the sample chamber. After OC was performed, the inspection laser, guided along the x axis by mirrors and focused into the sample using a 10x high damage threshold microscope objective (N.A. = 0.25, LMH-10X-1064, ThorLabs, USA) with energies varying between 150 mJ (minimum energy required to produce Cu signal at every laser event) and 260 mJ (maximum laser output), corresponding to a F range between 400 and 800 J/cm^2 at the sample spot. Sampling rate

was set to 1 Hz in order to minimize the impact of particle blowing due to plasma shockwave expansion upon the real hit % and avoid damaging the walls of the sample chamber. The E and, subsequently, sampling rate used herein were chosen on the basis of maximizing the direct observation of Cu signal and simplify data processing schemes while preserving the integrity of the sample chamber. Higher data acquisition throughput and lower E values should be feasible via the implementation of conditional data analysis pathways as described in reference [11]. Both lasers were actioned and synchronized using an external pulse generator, this provided enough time for the particle stream to reach the focal point of the LIBS laser and populate the interaction area. Successive OC pulses re-suspended aerosolized material and re-ejected sample deposited at the chamber's bottom. A TEM 00, 532 nm CW laser (MGL-DS-532, CNI, China) was used for visual observation of the generated particle streams.

LIBS signal collection was set in the y-axis (**Fig. 1C**) and consisted of a pair of planoconvex lenses (UV-FS, 100 focal length, 2" diameter) which focused the plasma light on the tip of a 600 μm and 0.22 N.A. optical fiber connected to a time-resolved Czerny-Turner spectrometer (Shamrock SR-303i, 250 mm focal length, 10 μm entrance slit, Andor, UK). A 300 lines/mm grate was employed to record emission in the 300-550 nm wavelength range. The spectrometer was coupled to an intensified camera (iCCD, DH734-18F-03, Andor, UK). For hyperspectral imaging, another iCCD (AndorIstar DH334T, 2048x2048 pixels, Andor, UK) also located in the y axis was used. As depicted in **Fig. 1C**, Plasma light in the xz plane passed, in first place, through a short-pass filter (F1) only allowing light in the 310-375 nm range to continue its path towards the camera, then, the light was focused by an UV-FS 1" biconvex lens of 50 mm focal length into a second wavelength-discrimination filter (F2). F2 was a line filter tilted 5 degrees in order to exclusively allow light at 324.75 nm to reach the detector. Despite the increased

number of photons lost as a consequence of using two filters, this was necessary as F2 also allowed light above 400 nm to pass through it, thus justifying the need of also placing F1 in the hyperspectral line.

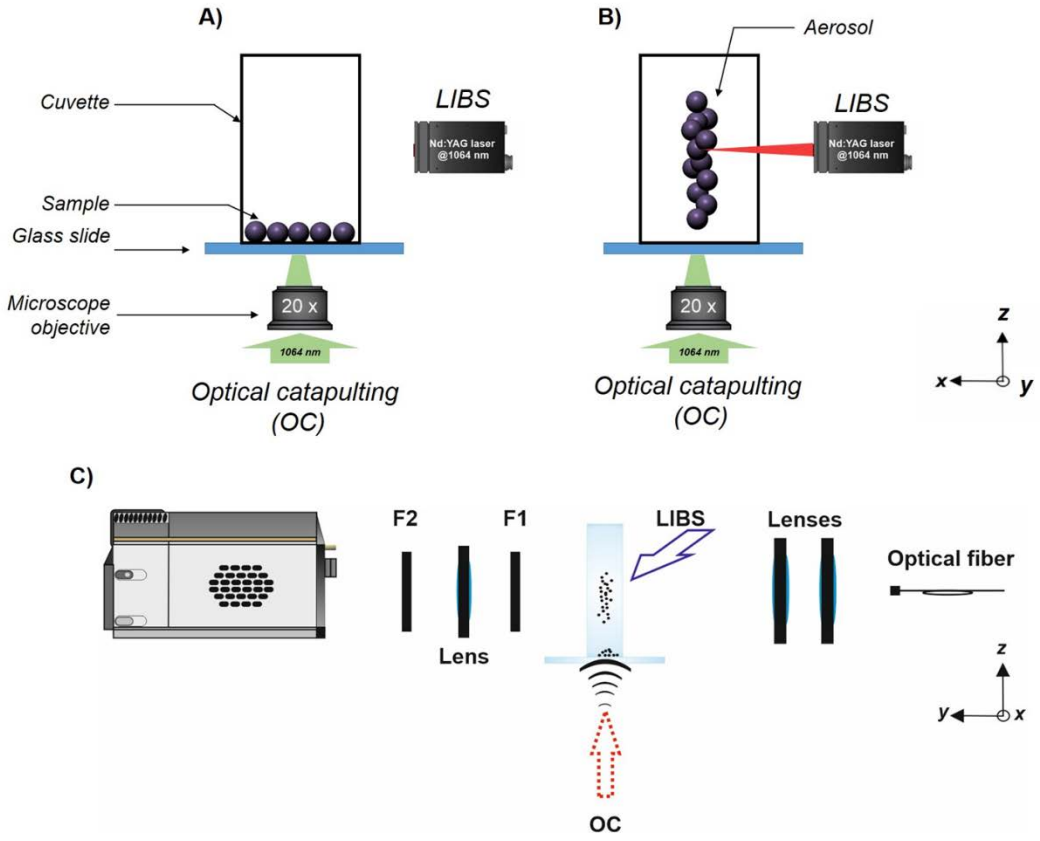

Figure 1.Experimental setup. Vignettes A and B illustrate the formation of dry aerosol streams via OC (A) and subsequent LIBS inspection (B). C) Optical layout for hyperspectral imaging. Appropriated reference axes are provided as described in the main text.

2.2. Samples

Qualitative portions ($m < 5x10^{-3}$ g) of Cu nanospheres of 25±3.7, 50±7.5 and 70±10.5 nm (MkNano, Canada) were used for the experiments ran in this work. Samples were placed upon 200 μm-thick glass slides and the covered by a quartz cuvette of 10 mm optical path (41 mm length) glued to the slide. This sample chamber was akin to that reported in references [18-21] and [23], yet, using quartz instead of plastic disposable cuvettes allowed for an increased chamber lifetime owed to a higher damage threshold of

the walls and for a larger number of photons to exit the cuvette. The total volume of air occluded within the sample chamber, as used in subsection 3.3 to calculate NP concentration, was 4.1 cm^3. Manipulation of the samples and chambers was performed using gloves to avoid possible wall contamination and subsequent signal loss. Controlled masses were weighed in an analytical balance for experiments described in subsection 3.3. Inspection was always performed in air, at atmospheric pressure and room temperature.

3. Results and discussion

3.1. Temporal evolution of the recorded LIBS signal in copper nanoaerosols. Electronic temperatures points towards relevant influence of seeding effects

Nanoparticles are known to yield quick-decaying signals in LIBS spectra with the exact intensity vs time behavior being related to the particle diameter [22, 26]. In order to evaluate the optimum time frame for aerosol inspection, we first evaluated the evolution of the LIBS signal in the Cu nanoaerosols. **Figure 2** plots the Cu (I) signal intensity at 324.75 nm, the most commonly used Cu line for NP monitoring [21, 24], as a function of the acquisition delay time for the three inspected particle sizes. Each point shown on the graph is the average of 15 laser events. The gate width for signal recording was 250 ns, acquisition delay was increased in 250 ns steps from d = 0 until the line SNR dropped below SNR = 3. The laser pulse energy was kept at 260 mJ/pulse based on previous experience [19].

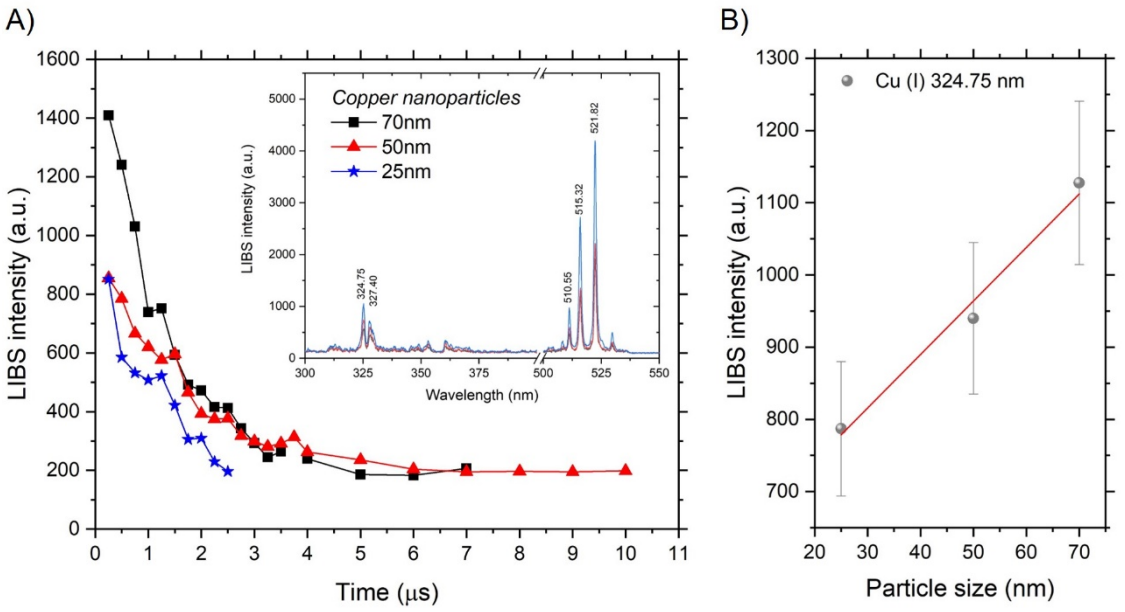

Figure 2. A) Temporal evolution of the LIBS signal for aerosols containing Cu NPs of 25, 50 and 70 nm in diameter. The plotted points are the average of 15 different laser events acquired at each time. Data were acquired every 250 ns starting from d = 0 up until signal extinction and the integration time was kept at 250 ns. As an example, the inset shows the average LIBS spectra acquired at d = 1000 ns featuring no line saturation. B) Correlation found between LIBS intensity of the Cu (I) at 324.75 nm and particle size for data shown in the inset in Fig. 2A.

As shown, the trend followed by each of the inspected Cu NP diameters was similar, an exponential decrease from the moment of plasma ignition. The lifetime of the smaller NP size was 64% shorter than the other two with the signal becoming extinct 4.5 μs earlier. On the other hand, from d = 2 μs, the 50 and 70 nm particles exhibited an identical evolution up to the 7 μs time mark, from which signal was lost. For in-bulk LIBS signal is mainly dependent on the ablated mass [25-27], yet, excitation efficiency plays a major role in particulate material analysis [18, 20-22]. The masses for the three NP sizes featured in this experiment was 1.61 fg, 0.59 fg, and 0.07 fg for the diameters of 70 nm, 50 nm, and 25 nm, respectively. This implies mass differences of up to ca. 23-fold when 70 nm particles are compared to the 25 nm ones. Despite the large mass differences found between the NPs, the net signals in **Fig. 2**, while proportional to sample size as illustrated

in the inset of **Fig. 2A**, did not show such drastic differences, with I_{Cu70} being only 1.6 times that of I_{Cu25} at d = 0. In consequence, this allowed for a good linear correlation between particle size and the signal collected at d = 1 μm, which featured the best SNR for the monitored 324.75 nm Cu line for each NP size, as presented in **Fig. 2B**. The observed linearity points towards the full dissociation of the inspected particles in the laser-produced plasma as expected for particles below 150 nm in diameter [22] while also hinting a high excitation efficiency for the smaller particles.

In order to delve deeper into the conclusions drawn from **Fig. 2**, electronic temperatures for the recorded plasmas were calculated from data plotted in the former graph. Blotzmann plots were used to obtain the value of Te for each particle size using Equation 1:

$$Ln\left(\frac{\lambda_{mn}\cdot I_{mn}}{A_{mn}\cdot g_m}\right) = Ln(h\cdot c\cdot N_e) - \frac{E_m}{K\cdot T_e} \qquad \text{(Eq.1)}$$

where λ_{mn} is the wavelength of the considered transit, I_{mn} is the intensity of the line, A_{mn} is the transition probability, g_m is the statistic weight of the upper state, h is Plank's constant, c is the speed of light, N_e is the electronic density, E_m is the energy of the upper state an k is the Boltzmann constant. Exact values used for Te calculus are given in **Table 1**. Figure 3A shows an example of the resulting Boltzmann plots for each Cu NP at d = 1000 ns. From the slopes in the plot, Te are calculated, resulting in Te_{25} = 12105 K, Te_{50} = 11781 K and Te_{70} = 11458 K. Upon extraction of the Te values at every delay value shown in Fig. 3A, the temporal evolution of the parameter was studied as a function of particle diameter. Results are provided in Fig. 3B with Te values being consistently higher the smaller the particle size was along the plasma lifetime. A potential explanation for these results arises from the seeding effect observed for NPs in laser induced plasmas. Whenever an aerosol stream was created in our setup, a number of ejected particles

populated the focal volume, i.e. the space in which laser-NP interaction occurred. While the focal volume remained constant throughout the experiments, the number of particles could oscillate owed to the different volume each of the inspected sizes occupy, with this volume being V_{25} = $8.18 \cdot 10^{-18}$ cm^3, V_{50} = $6.54 \cdot 10^{-17}$ cm^3 and V_{70} = $1.79 \cdot 10^{-16}$ cm^3. Therefore, assuming a completely filled interaction volume (I.V. = $1.13 \cdot 10^{-4}$ mm^3) at a same moment in time, the number of particles present within it was larger the smaller the particles were. As more absorbing entities were present in the optical path, thus enabling a larger fraction of the incoming laser pulse energy to be absorbed and used to create several hot plasma nuclei that synergistically contribute towards an overall hotter plasma. Plasma formation threshold energies (E_{th}), defined as the minimum pulse E required to observe Cu signal in 8 out of every 10 recorded spectra, were calculated as a function of size to corroborate this hypothesis. E_{th} were 134 mJ for 25 nm NPs and 143 mJ for 50 and 70 nm NPs, confirming stronger seeding effects for smaller particle sizes. The thermal energy held by the plasma also contributes to the dissociation and further excitation of the NPs, therefore justifying the relatively high signal observed for 25 nm NPs. Moreover, the lower Te found for 70 nm NPs could be indicative of the larger energy required to fully atomize the particles, leading to colder nuclei and restricted interaction between the nodes.

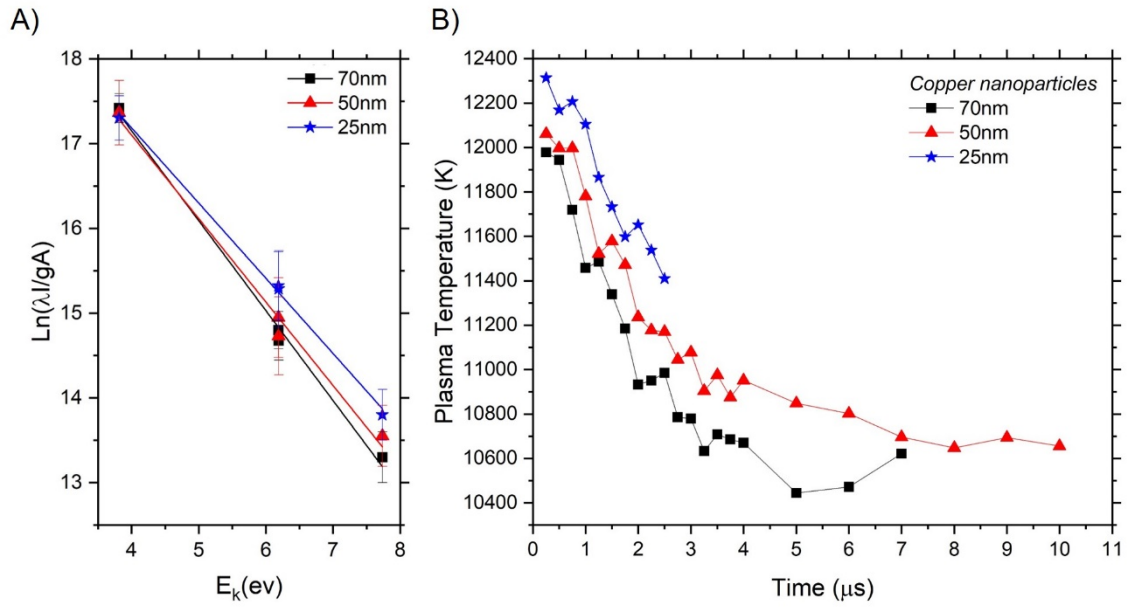

Figure 3. A) Example Boltzmann plot for Cu data recorded at d = 1000 ns and gate width = 250 using equation 1. B) Evolution of the plasma electronic temperature as a function of time using data in Fig. 2A. Each point shown is the average of 15 Te values corresponding the 15 laser events in the mentioned figure.

Table 1. Values of the parameters used in Eq.1 to extract the Te values of the Cu NPs plasmas shown in Fig. 3.

λ (nm)	**Lower level energy (E_n) (cm^{-1})**	**Upper level energy (E_m) (cm^{-1})**	**g_m**	**A_{mn} (10^8 s^{-1})**
324.75	*0*	*30783.70*	4	1.395
327.39	*0*	*30535.32*	2	1.376
510.50	*11202.62*	*30783.70*	4	0.02
515.29	*30535.32*	*49935.19*	4	0.6
521.82	*30783.70*	*49942.05*	6	0.75

In the experiments performed, the Cu emission line at 324.75 nm was detected in all the recorded events, which implies a detection efficiency of 100%, thus circumventing the use of conditional analysis. In addition, the signal variability was of 20% RSD for Cu_{70} NPs, 21% RSD for Cu_{50} NPs and 23% RSD for Cu_{25} NPs. The calculated uncertainties were consistent with differently populated interaction volumes, which is typical in LIBS inspection of aerosols as the shockwave produced when a plasma is ignited and expands is capable of blowing material far away from the probed volume leading to a variable number of particles being occluded in each of the sparked plasmas [28]. As demonstrated in literature, blowing effects can be prevented at the expense of longer analysis times by indirect inspection of the aerosol (e.g. particle collection in filters) [24], while conditional analysis at lower pulse energy values might improve RSDs for direct inspection should the excitation parameters be adjusted as required [11].

These results indicate the strong dependence of ultrafine aerosol analysis on the chosen collection time frame with the optimal window becoming narrower with particle size, yet highlight the capability of LIBS to work on a qualitative level with these samples as the mechanisms responsible for signal generation favor the detection of smaller particles.

3.2. Hyperspectral analysis evidences the excitation mechanism and explains measured signal fluctuations

In LIBS analysis of aerosols and particulate matter, two main mechanisms are widely accepted to cause the dissociation and atomization of the nanoparticle, (i) laser-particle interaction and (ii) plasma-particle interaction. Although both mechanisms are concomitant, the prevalence of one over the other may lead to severe differences in the recorded spectra. As an extreme example of this notion, a non-optimized inspection of a process dominated by plasma-particle interaction may lead to signals of interest being

totally concealed within the emission of excited air species [18]. Plasma imaging has been a powerful tool in order to discern and describe essential knowledge pertaining to LIBS aerosol inspection such as the predominant process [28] or to expose the sources causing spectral fluctuations. To back and expand the conclusions drawn from the experiments described in section 3.1 while assessing the role of fundamentals taking place in our proposed experimental scheme, hyperspectral imaging was performed with simultaneous and coincidental LIBS detection. Wavelength-resolved images shown in **Fig. 4A** monitor emission the Cu (I) line at 324.75 nm in plasmas containing 70 nm Cu NPs using fixed hyperspectral and LIBS acquisition parameters (d = 1000 ns, gate width = 250 ns) along a sequence of 15 laser events recorded with a 1 Hz repetition frequency. Images were normalized to the maximum hyperspectral intensity value, which corresponds to laser event #8. As observed, during the first two events, the interaction volume was progressively populated by catapulting events. Event #3 evidences the high directionality of the aerosol streams produced by OC as only one well-defined and localized plasma core was observed. As more particle arrived at the inspection laser's focus and recirculate the sample chamber, the width of the plasma expanded, eventually reaching a sufficient number of particles to make seeding effects observable as evidenced by the small hot spots already visible in event #4 and the intensity spike and the two hot cores in event #5. The formation of multiple hot spots is tied to a stronger plasma shockwave capable of pushing the surrounding NPs to the walls of the chamber and out of the focal region, this explaining the slight intensity drop in event #6 as well as the formation of two tails at the front (the laser propagation direction) and the rear of the plasma. The larger spatial dispersion agreed with the better nuclei separation observed in event #7 which, despite being smaller in size, retained the hyperspectral intensity of event #6 as, in time, more particles reached the probed volume. Event #8 once again exhibited strong seeding effects

and gave way to a new cycle of NP blowing-repopulation which continued throughout the following recorded events as seen in events #11 and #12-#15. From event #8, hyperspectral signal became steadier and less intense cores were register probably due to higher spatial dispersion of the NPs, which was coherent with the better-separated plasma lobes found in the mentioned #12-#15 series.

As shown in **Fig. 4B**, simultaneous LIBS intensity of the 324.75 nm correlated entirely to the image at each of the events, thus supporting the rationale of the phenomena taking place within the recorded series and the existing synergy of hot spots towards yielding more intense signals. Inhomogeneous plasma morphology, absence of cold peripheries [28] or quantifiable plasma size reductions [22] and intensity spikes coherent with NP fill/exhaust cycles at the in$_{te}$raction volume, imply that laser-particle interaction was predominant as intensity was mainly related to the number of absorbing NPs present at the time of probing. Moreover, correlated analysis using two different detection methods unambiguously marked interaction volume exhaustion as the main source of signal variability. Still, lower RSDs reported herein suggest that dry aerosol recirculation through the sample chamber paves the way towards enhancing analysis of nanoaerosols using LIBS without requiring pre-concentration stages. Also, in **Fig. 4B**, the Cu (I) emission at 521.82 nm was monitored to compare the analytical performance of both lines. If we focus on the first events (from #1 to #4), the behavior of this emission significantly deviates from the Cu (I) emission at 324.75 nm. Literature reports a preferential population of transits low-lying upper states for single NP analysis [20-21]. The emission lines at 510.50, 515.29, and 521.82 nm correspond to transitions from one excited state to another, while the emission lines at 324.75 and 327.39 nm start from the ground state. Therefore, in the first events, when the particle density in the focal volume was lower, the energy was primarily invested in the excitation of transits involving the

324.75 and 327.39 nm lines. After the levels involved in these transitions were populated, the remaining energy fraction was then invested in populating higher energy states, i.e., the transitions at the visible region, explaining the correlation between lines from pulse #5 onwards with the 521.74 nm line showing a higher RSD.

A)

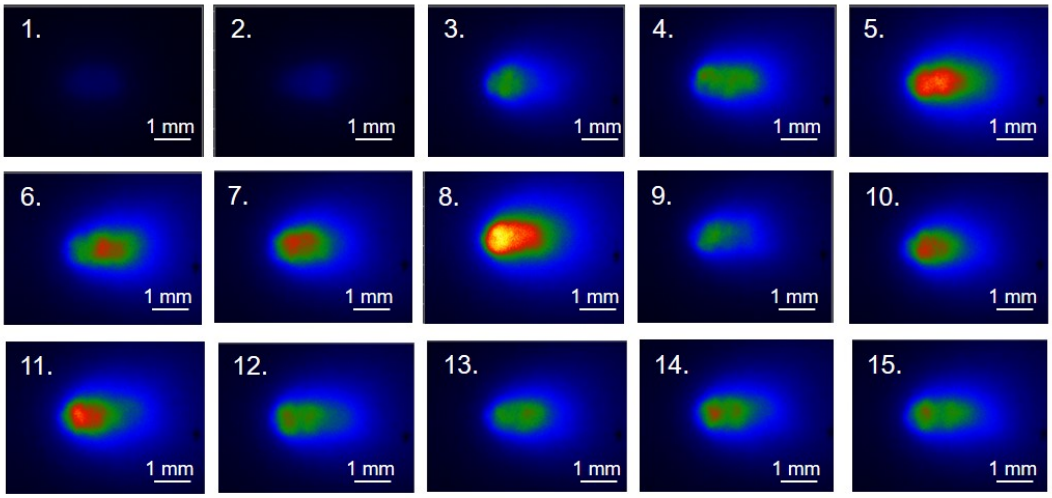

B)

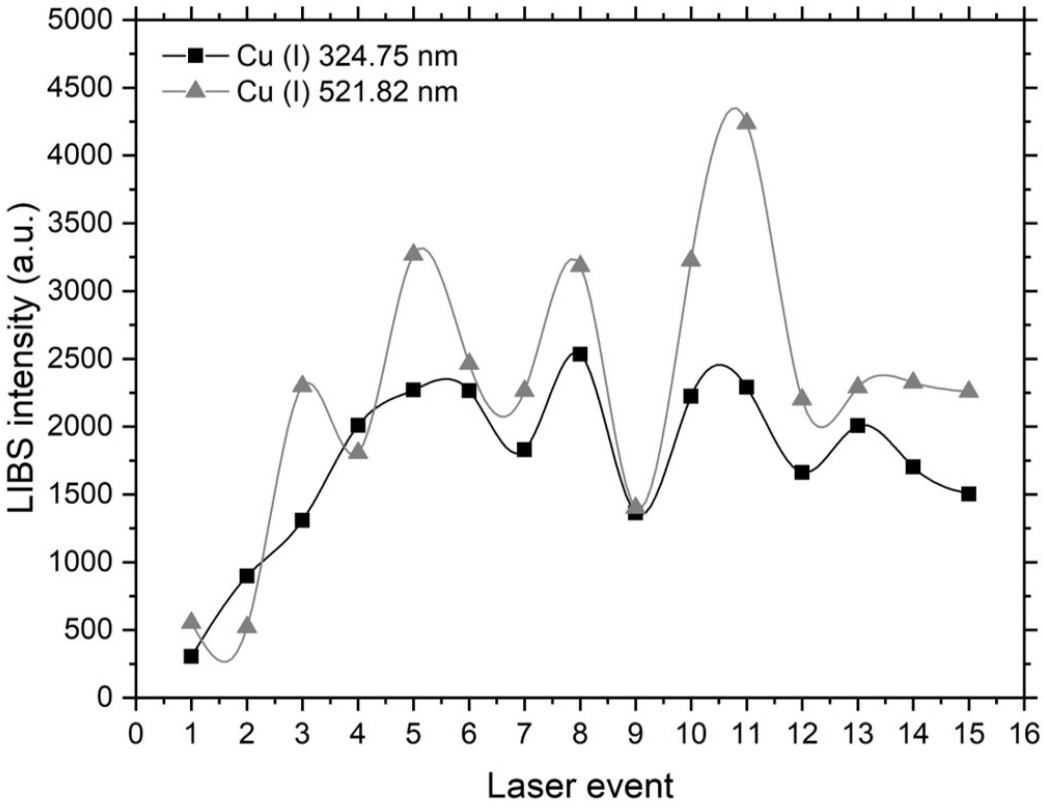

Figura 4. A) Hyperspectral images featuring emission belonging to the Cu (I) 324.75 nm line along 15 laser events on 70 nm Cu NPs. B) LIBS intensity of the Cu (I) lines at 324.75 nm and 521.82 nm corresponding to each of the laser events shown in A. Energy was kept at 260 mJ per pulse. From event 5 onwards population/exhaustion cycles occur yielding stable signal on successive events. This, alongside 100% real hit rate, avoided the need of acquiring hundreds of spectra to characterize the aerosol.

In **Fig. 4B**, an inversion of the LIBS intensity ratio between both monitored lines occurred, this raised the interest in evaluating the influence of the analyzing laser on the LIBS signal and drawing a comparison between the linear ranges. **Figure 5** shows the intensity at 324.75 nm and 521.82 nm as a function of the laser beam energy for 25, 50 and 70 nm Cu nanoparticles. Intensity was normalized to the corresponding maximum LIBS intensity along the scanned E values for each Cu (I) line. LIBS spectra were recorded at optimum acquisition settings. The energy working range was 150-260 mJ/pulse. In all cases, the signal at 324.75 nm reached a maximum value, after which it started to decrease. On the contrary, the signal corresponding to the transit at 521.82 nm increased progressively for higher laser beam energies. Both signals intersected at a size-dependent energy value from which the intensity ratios reversed as shown in **Fig. 6**. Inversion in the intensity ratios occurred at lower pulse energy values the smaller the NP size was, that being 205 mJ/pulse for the 25 nm NPs, 235 mJ/pulse for the 50 nm NPs and approximately 245 mJ/pulse for the 70 nm NPs. A plausible explanation to the observed ratio inversion sources from the expected Te for each particle size at those specific energies. As discussed above, the electronic temperature of the laser-produced plasmas was consistently larger for smaller NPs owed to seeding effects. Both UV lines are bound to saturate earlier than the VIS lines since low-lying levels are preferentially populated. Upon filling of the excited state at 324.75 nm, the higher electron density featured by hotter plasmas then caused the emission to self-absorb [29], thus modifying its proportionality to excitation energy and, eventually, leading to signal decay. This

explanation is further reinforced by the well-known increased sensitivity that UV lines possess towards self-absorption as a result of their resonant nature. Ensuing results from these experiments indicated that the linear range for the UV transit increased with NP size, with VIS lines turning into a better option for monitoring smaller diameters. It is therefore clear that plasma physical traits and the nature of the monitored transit are to be carefully considered as a function of expected particle size for the implementation of LIBS in quantitative ultrafine aerosol studies.

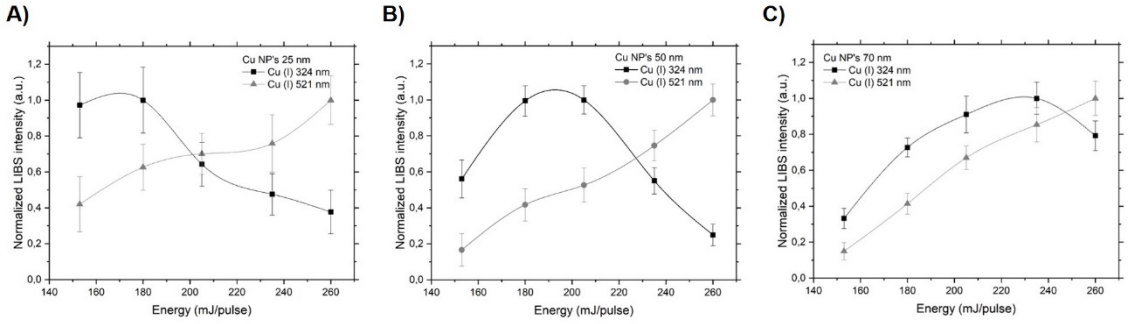

Figure 5. Normalized Cu intensity at 324.75 and 521.82 nm as a function of the laser beam energy for the different particle sizes, A) 25 nm, B) 50 nm, and C) 70 nm. In all cases, the LIBS spectra were acquired at d = 1000 ns and gate width = 250 ns. The more prominent seeding effect observed in smaller particle sizes was responsible of the high signal observed at low E values for 25 nm NPs

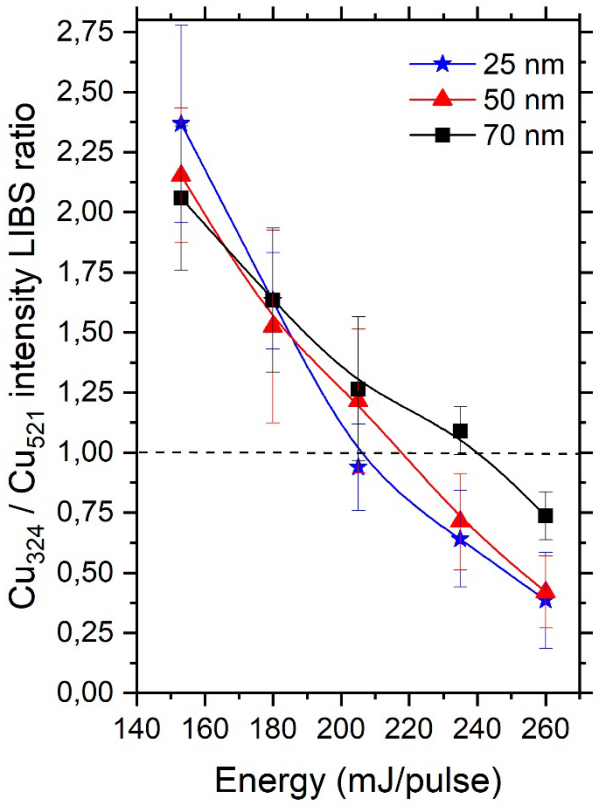

Figure 6. LIBS 324.75/521.82 intensity ratios as a function of the inspection laser beam energy.

3.3. LIBS inspection of controlled NP mass portions for selecting the optimum emission to monitor in ultrafine aerosols

Fieldable LIBS sensors for aerosol inspection tend to work using pulse energy values close to the maximum output of the employed laser, usually in the range of hundreds of mJ and up to ca. 1 J. The differences observed between the intensity of the 324.75 nm and the 521.82 nm Cu (I) lines as a function of the energy of the inspection pulse arise doubts concerning the suitability of these lines for quantitative-focused approaches as well as for particle sizing. To understand how the particle density affects the LIBS response, known masses of each of the three available Cu NP samples ranging from 1.5 mg to 16 mg were subjected to OC-LIBS. The upper mass limit was chosen after observing consistent signal saturation, from which accurate sensors' performance is groundless. In these experiments, pulse energy was kept at 260 mJ with acquisition

parameters being identical to those employed in the subsection above. Intensities for both monitored lines as a function of the weighed mass placed of the aerosolized sample are plotted in **Fig. 7A**. For all particle sizes studied, an increasing trend was observed up to ca.10 mg, from which, the intensities decreased, indicating saturation of both signals likely due to excess mass present at the interaction volume. Interestingly, for the lower masses inspected (1.5-3.5 mg), the 324.75 nm line was more stable, especially for 50 nm and 25 nm NPs. The concentration ranges in NPs per cm^3 corresponding to the stated masses were $2.72 \cdot 10^{14}$ - $5.30 \cdot 10^{14}$ NP/cm^3 (70 nm NPs), $6.24 \cdot 10^{14}$ – $1.45 \cdot 10^{15}$ NP/cm^3 (50 nm NPs) and $5.01 \cdot 10^{15}$ – $1.17 \cdot 10^{16}$ (25 nm NPs) NP/cm^3, confirming that up to and order of magnitude more particles can be present at the focal region upon LIBS inspection. Suitability of the UV line for lower NP concentrations could be due to the preferential population of low-lying upper levels being more prominent in the case of limited number of atoms [20]. Figure 7B plots the ideal correlation between intensity and absolute sample mass before signal collapse for each particle size. From these graphs, Cu (I) line at 324.75 nm appeared to be a better choice for monitoring low NP masses, i.e. below 2 mg, as its response was consistently higher that of the visible line, in agreement with the argument of preferential population. Yet, for higher NP quantities, the 521.82 nm emission offers a better sensitivity, as evidence by its steeper slope, indicating that, in the higher NP density ranges (corresponding to masses ca. 3.5-7.5 mg in our case), this line may be of greater interest mainly due to its lower predisposition towards self-absorption. Moreover, larger signal differences alongside intensity ratios between lines at 510.55 nm, 515.32 nm and 521.82 nm should be useful to ascertain whether discrete or clustered NPs are being examined as, according to recently reported data [22], the latter results in reversed 521.82/510.55 nm ratios. It is worth noting that the quantities employed herein were high, facilitating detectability at laboratory scale. Lower particle

densities along with the occlusion of particles within water droplets are common in off-lab conditions, therefore, further work is to be performed to address the response of the UV and the Vis lines in those cases.

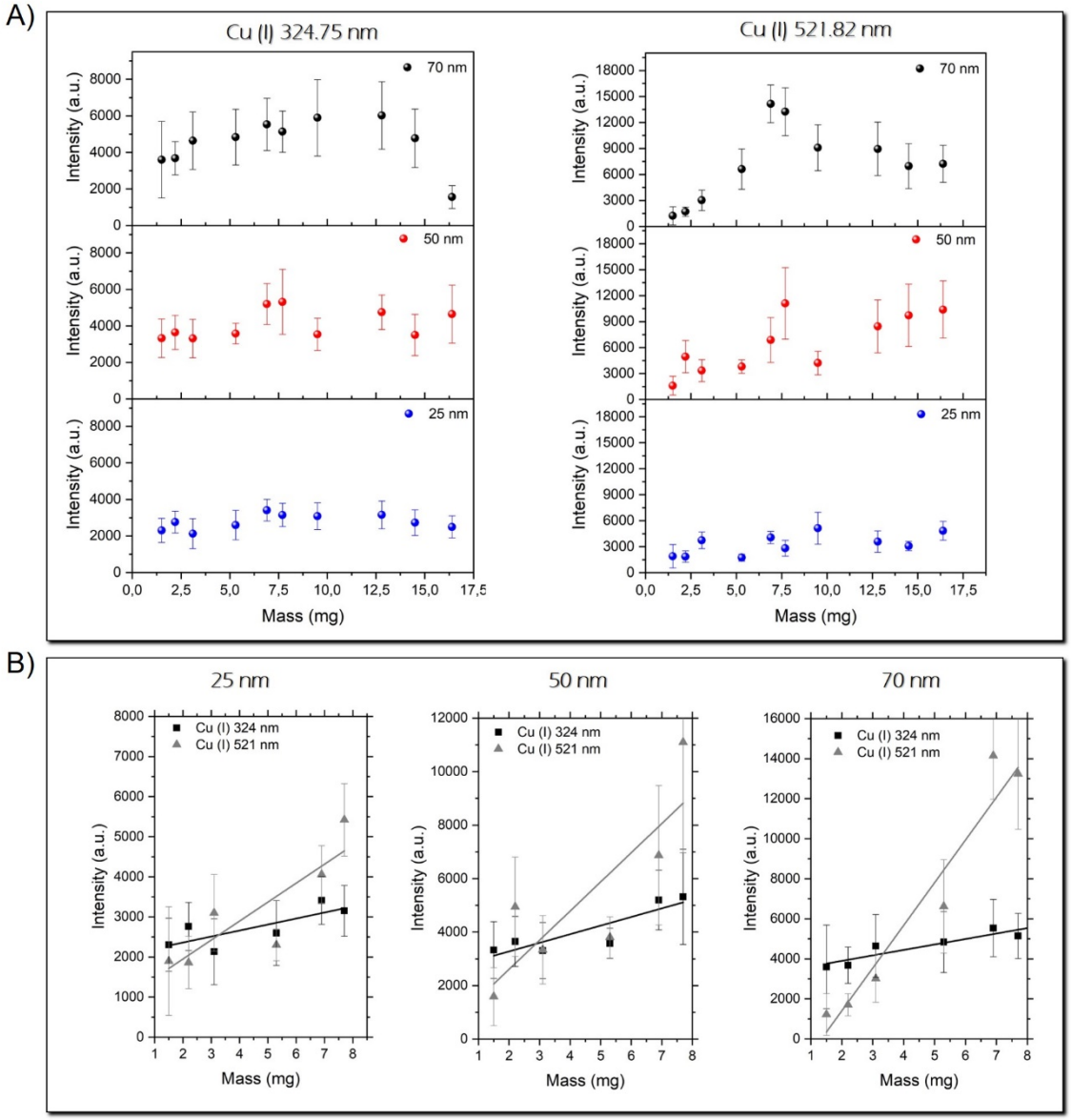

Figure 7. A) LIBS intensity for the 324.75 nm and 521.82 nm Cu (I) lines as a function of the NP mass placed within the sample chamber. Spectra were acquired at E = 260 mJ/pulse. B) Linear fits for data from 1.5 mg up to 9.5 mg in A. Signal recorded thereafter exhibited saturation and where, therefore, discarded for calibration.

4. Conclusions

Dry Cu nanoparticles with sizes ranging from 25 nm to 70 nm in diameter were aerosolized by optical catapulting (OC) within a sample chamber and then probed by time-resolved LIBS. Plasma lifetime was demonstrated to increase proportionally to particle size whereas plasma electronic temperature was exhibited the opposite behavior, that it is, decreased with size. Higher Te values for smaller particles is due to the seeding effect caused by the larger number of entities interacting with the excitation laser beam and absorbing part of the radiation present at the volume probed by the laser. For confined aerosols, the observed LIBS intensity RSD values was tied to cyclic population/exhaustion of the focal region as demonstrated by time-resolved hyperspectral imaging and coincidental LIBS spectroscopy. After a number of OC events formed a sufficiently particle-dense aerosol, seeding effects occurred yielding a plasma featuring increased emission intensity. The stronger shockwave linked to this plasma blew the particles away from the focus, thus decreasing the intensity of subsequent events until the interaction volume was repopulated, thus explaining signal fluctuations. Hyperspectral imaging also allowed to observe the formation of several plasma cores whose synergistically positive interaction resulted in enhanced collected signals. The parallel behavior of the Cu (I) line at 324.75 nm (monitored in hyperspectral imaging) and the Cu (I) line at 521.82 nm confirmed this conclusion and sparked the interest in understanding which emission was more appropriated for ultrafine aerosol inspection. The 324.75/521.82 intensity ratio inverted upon increasing the energy of the inspection pulse, evidencing particle size-dependent linear ranges for each line. A plausible explanation for this was found in the tendency towards saturation of the UV line with higher plasma electron temperature. Measures under controlled absolute mass portions of the NPs highlighted the UV line as better option signal-wise for low concentrations of particles, yet the emission at 521.82 nm featured overall better sensitivity with mass, thus becoming

a stronger asset for quantitative studies of airborne material with diameters lower than 100 nm.

Author Contributions

F.J.F. and P.P. designed the experiments with input and supervision from J.J.L. F.J.F., I.M and L.J-F. carried out the reported experiments. All authors contributed to data processing and interpretation. The first manuscript draft was written by P.P. and L.J-F.with further versions featuring contributions by all authors. All authors have approved the final version of the document.

Notes

Authors declare no competing financial interest.

Acknowledgments

Research funded by the Spanish Ministerio de Economia y Competitividad under Projects CTQ2017-82137P and CTQ2014-56058P. Pablo Purohit would also like to acknowledge the Junta de Andalucia for his contract under the program “Garantía Juvenil”.

REFERENCES

[1] J. Huang, X. Pan, X. Guo, G. Li, Health impact of China's air pollution prevention and control action plan: an analysis of national air quality monitoring and mortality data, Lancet Planet. Heal. 2 (2018) e313–e323. https://doi.org/10.1016/S2542-5196(18)30141-4.

[2] W.J. Gauderman, R. Urman, E. Avol, K. Berhane, R. McConnell, E. Rappaport, R. Chang, F. Lurmann, F. Gilliland, Association of improved air quality with lung development in children, N. Engl. J. Med. 372 (2015) 905–913. https://doi.org/10.1056/nejmoa1414123.

[3] M. Darçın, Association between air quality and quality of life, Environ. Sci. Pollut. Res. 21 (2014) 1954–1959. https://doi.org/10.1007/s11356-013-2101-3.

[4] D. Diaz, D.W. Hahn, U. Panne, LIBS for aerosol analysis, in: J.P. Singh, S.N. Thakur (Eds.), Laser-induced breakdown spectroscopy, Elservier Science, Amterdam, 2020, pp. 499-536. https://doi.org/10.1016/b978-0-12-818829-3.00022-8.

[5] J. Laserna, J.M. Vadillo, P. Purohit, Laser-induced breakdown spectroscopy (LIBS): fast, effective, and agile leading edge analytical technology, Appl. Spectrosc. 72 (2018) 35–50. https://doi.org/10.1177/0003702818791926.

[6] F.J. Fortes, J. Moros, P. Lucena, L.M. Cabalín, J.J. Laserna, Laser-induced breakdown spectroscopy, Anal. Chem. 85 (2013) 640–669. https://doi.org/10.1021/ac303220r.

[7] M.S. Afgan, S. Sheta, Y. Song, W. Gu, Z. Wang, Improved signal stability using an auxiliary flow-based chamber for aerosol laser-induced breakdown spectroscopy,

Spectrochim. Acta - Part B At. Spectrosc. 180 (2021) 106204. https://doi.org/10.1016/j.sab.2021.106204.

[8] D.J. Palásti, A. Metzinger, T. Ajtai, Z. Bozóki, B. Hopp, Kovács-Széles, G. Galbács, Qualitative discrimination of coal aerosols by using the statistical evaluation of laser-induced breakdown spectroscopy data, Spectrochim. Acta - Part B At. Spectrosc. 153 (2019) 34–41. https://doi.org/10.1016/j.sab.2019.01.009.

[9] P.K. Diwakar, K.H. Loper, A.-M. Matiaske, D.W. Hahn, Laser-induced breakdown spectroscopy for analysis of micro and nanoparticles, J. Anal. At. Spectrom. 27 (2012) 1110. https://doi.org/10.1039/c2ja30012e.

[10] D.W. Hahn, M.M. Lunden, Detection and analysis of aerosol particles by laser-induced breakdown spectroscopy, Aerosol Sci. Technol. 33 (2000) 30–48. https://doi.org/10.1080/027868200410831.

[11] D. Diaz, D.W. Hahn, Aerosol measurements with laser-induced breakdown spectroscopy and conditional analysis, Spectrochim. Acta - Part B At. Spectrosc. 179 (2021) 106107. https://doi.org/10.1016/j.sab.2021.106107.

[12] J.E. Carranza, K. Iida, D.W. Hahn, Conditional data processing for single-shot spectral analysis by use of laser-induced breakdown spectroscopy., Appl. Opt. 42 (2003) 6022–8.

[13] D. Girón, T. Delgado, J. Ruiz, L.M. Cabalín, J.J. Laserna, In-situ monitoring and characterization of airborne solid particles in the hostile environment of a steel industry using stand-off LIBS, Measurement. 115 (2018) 1–10. https://doi.org/10.1016/j.measurement.2017.09.046.

[14] V. Riffault, J. Arndt, H. Marris, S. Mbengue, A. Setyan, L.Y. Alleman, K. Deboudt, P. Flament, P. Augustin, H. Delbarre, J. Wenger, Fine and ultrafine particles in the vicinity of industrial activities: a review, Crit. Rev. Environ. Sci. Technol. 45 (2015) 2305–2356. https://doi.org/10.1080/10643389.2015.1025636.

[15] F.J. Fortes, L.M. Cabalín, J.J. Laserna, Laser-induced breakdown spectroscopy of solid aerosols produced by optical catapulting, Spectrochim. Acta - Part B At. Spectrosc. 64 (2009) 642–648. https://doi.org/10.1016/j.sab.2009.05.006.

[16] F.J. Fortes, J.J. Laserna, Characteristics of solid aerosols produced by optical catapulting studied by laser-induced breakdown spectroscopy, Appl. Surf. Sci. 256 (2010) 5924–5928.

[17] M. Abdelhamid, F.J. Fortes, M. a. Harith, J.J. Laserna, Analysis of explosive residues in human fingerprints using optical catapulting–laser-induced breakdown spectroscopy, J. Anal. At. Spectrom. 26 (2011) 1445.

[18] P. Purohit, F.J. Fortes, J.J. Laserna, Atomization efficiency and photon yield in laser-induced breakdown spectroscopy analysis of single nanoparticles in an optical trap, Spectrochim. Acta Part B At. Spectrosc. 130 (2017) 75–81. https://doi.org/10.1016/j.sab.2017.02.009.

[19] P. Purohit, F.J. Fortes, J.J. Laserna, Spectral identification in the attogram regime through laser-induced emission of single optically trapped nanoparticles in air, Angew. Chemie - Int. Ed. 56 (2017) 14178–14182. https://doi.org/10.1002/anie.201708870.

[20] P. Purohit, F.J. Fortes, J.J. Laserna, Subfemtogram simultaneous elemental detection in multicomponent nanomatrices using laser-induced plasma emission spectroscopy within atmospheric pressure optical traps, Anal. Chem. 91 (2019) 7444–7449. https://doi.org/10.1021/acs.analchem.9b01579.

[21] P. Purohit, F.J. Fortes, J.J. Laserna, Optical trapping as a morphologically selective tool for in situ LIBS elemental characterization of single nanoparticles generated by laser ablation of bulk targets in air, Anal. Chem. 93 (2021) 2635–2643. https://doi.org/10.1021/acs.analchem.0c04827.

[22] F.J. Fortes, P. Purohit, J.J. Laserna, Energy transfer mechanisms in laser-induced plasmas: variation of physical traits mediated by the presence of single optically-trapped nanoparticulate material, Spectrochim. Acta Part B At. Spectrosc. 180 (2021) 106193. https://doi.org/10.1016/j.sab.2021.106193.

[23] F.J. Fortes, A. Fernández-Bravo, J. Javier Laserna, Chemical characterization of single micro- and nano-particles by optical catapulting-optical trapping-laser-induced breakdown spectroscopy, Spectrochim. Acta - Part B At. Spectrosc. 100 (2014) 78–85.

[24] G. Gallou, J.B. Sirven, G. Gallou, C. Dutouquet, O. Le Bihan, E. Frejafon, Aerosols analysis by libs for monitoring of air pollution by industrial sources, Aerosol Sci. Technol. 45 (2011) 918–926. https://doi.org/10.1080/02786826.2011.566899.

[25] M. Dell'Aglio, Z. Salajková, A. Mallardi, M.C. Sportelli, J. Kaiser, N. Cioffi, A. De Giacomo, Sensing nanoparticle-protein corona using nanoparticle enhanced laser induced breakdown spectroscopy signal enhancement, Talanta. 235 (2021). https://doi.org/10.1016/j.talanta.2021.122741.

[26] Z. Salajková, V. Gardette, J. Kaiser, M. Dell'Aglio, A. De Giacomo, Effect of spherical gold nanoparticles size on nanoparticle enhanced laser induced breakdown spectroscopy, Spectrochim. Acta - Part B At. Spectrosc. 179 (2021). https://doi.org/10.1016/j.sab.2021.106105.

[27] C. Koral, M. Dell'Aglio, R. Gaudiuso, R. Alrifai, M. Torelli, A. De Giacomo, Nanoparticle-enhanced laser induced breakdown spectroscopy for the noninvasive

analysis of transparent samples and gemstones, Talanta. 182 (2018) 253–258. https://doi.org/10.1016/j.talanta.2018.02.001.

[28] A. Botto, B. Campanella, S. Legnaioli, M. Lezzerini, G. Lorenzetti, S. Pagnotta, F. Poggialini, V. Palleschi, Applications of laser-induced breakdown spectroscopy in cultural heritage and archaeology: a critical review, J. Anal. At. Spectrom. 34 (2019) 81–103. https://doi.org/10.1039/C8JA00319J.

[29] V. Hohreiter, D.W. Hahn, Plasma-particle interactions in a laser-induced plasma: implications for laser-induced breakdown spectroscopy, Anal. Chem. 78 (2006) 1509–1514. https://doi.org/10.1021/ac051872s.

[30] A. Taleb, V. Motto-Ros, M.J. Carru, E. Axente, V. Craciun, F. Pelascini, J. Hermann, Measurement error due to self-absorption in calibration-free laser-induced breakdown spectroscopy, Anal. Chim. Acta. 1185 (2021). https://doi.org/10.1016/j.aca.2021.339070.